

# Electronic–Photonic Co-Optimization of High-Speed Silicon Photonic Transmitters

Sen Lin, *Student Member, IEEE*, Sajjad Moazeni, *Student Member, IEEE*,  
Krishna T. Settaluri, *Student Member, IEEE*, and Vladimir Stojanović, *Member, IEEE*

**Abstract**—System-level driven electronic–photonic codesign is the key to improving the bandwidth density and energy efficiency for high-speed silicon photonic links. In many data-communication scenarios, optical link power is dominated by its transmitter side including the laser source. In this paper, we propose a comprehensive co-optimization framework for high-speed silicon photonic transmitters utilizing compact models and a detailed optical simulation framework. Given technology and link constraints, microring and Mach–Zehnder transmitter designs are optimized and compared based on a unified optical phase shifter model. NRZ and PAM4 modulation schemes are analyzed and compared for microring-based transmitters at 50 Gb/s. Multistage and traveling wave Mach–Zehnder transmitters are optimized and discussed as well. The results show that, for a 50 Gb/s NRZ optical link, an optimized microring transmitter could save more than 60% of the total laser and driver power compared to an optimized Mach–Zehnder transmitter under equivalent photonic technology constraints. For a given data rate and receiver sensitivity, design tradeoffs of silicon photonic processes, devices, and architecture choices are discussed in depth. In addition, this paper introduces a new Simulink toolbox for transient optical simulation. Combined with the proposed optimization engine, it provides an electrooptical co-optimization approach toward truly energy-efficient high-speed silicon photonic links.

**Index Terms**—Circuits, modeling, modulator, optical links, optimization, silicon photonics, transmitter.

## I. INTRODUCTION

SILICON photonics holds great promise in replacing conventional optical interconnects and electrical interconnects in today's data centers as the bandwidth-length product demand keeps growing. Optical links based on silicon photonics are one of the most promising candidates for meeting the demands of next-generation 400 G inter-rack interconnects and 100 G intra-rack interconnects in data centers. To meet such demands, optical transceivers with data rates at or higher than 50 Gb/s are of the most interest in both wavelength-division multiplexed (WDM) and parallel single-mode (PSM) systems. Recent years

have seen great effort and rapid progress in the development and commercialization of silicon photonic technologies ranging from platforms, devices, circuits to large-scale systems [1]–[9]. Moreover, silicon photonic modulators and optical transceivers beyond 50 Gb/s have recently been demonstrated in various photonic platforms [10]–[15]. At these high data-rates it is critical to consider holistically the design of the photonic and circuit components from the perspective of link energy-efficiency and bandwidth density.

In state-of-the-art 50 Gb/s NRZ optical link based on Mach–Zehnder modulator (MZM), the driver and laser together consume more than 10 pJ/b energy dominating the total link energy, compared to 1.4–3 pJ/b consumed by the receiver [10], [11]. In contrast to MZMs, microring modulators (MRM) can consume less than 100 fJ/b driver energy due to their compact sizes. The thermal tuning overhead for microrings can be as low as a few milliwatts per channel [21], which has negligible impact on the overall energy efficiency of the transmitter. Microring modulators have great potential for dense WDM systems due to their inherent wavelength selectivity. They have also shown promising high-speed operations for single-wavelength 50 Gb/s links [12], [18]. However, full optical links at such high data rate using microring modulators are yet to be demonstrated, which is in part due to unoptimized device designs and the inherent trade-offs between optical modulation amplitude (OMA) and optical bandwidth for microrings [19]. For both types of modulators, there are different architecture choices and also trade-offs between laser power and transmitter power. Additionally, they are both subject to the same technology constraints from the silicon photonic platforms and link specifications. As a result, it is critical yet challenging to co-optimize photonics alongside circuits. To date, there is still debate on which modulator architecture could be a better design choice for 50 Gb/s optical channels in WDM and PSM systems.

This paper is intended to answer the questions above and provide new insights and intuition into high-speed silicon photonic transmitters. The paper focuses on a comparison between microring and Mach–Zehnder modulators given the same technology constraints at 50 Gb/s. We begin with an overview of the optimization framework in Section II and introduction of a compact model for phase shifters in Section III. The phase shifter model is verified with experimental data and later sets the foundation for microring and Mach–Zehnder modulator modeling. In Section IV, the optimization of the microring-based transmitter is carried out for 50 Gb/s optical links to obtain the

Manuscript received April 25, 2017; revised July 17, 2017 and September 14, 2017; accepted September 23, 2017. Date of publication September 28, 2017; date of current version October 25, 2017. This work was supported in part by the National Science Foundation ECCS under Grant 1611296, in part by Berkeley Wireless Research Center, and in part by DARPA POEM Program. (Corresponding author: Sen Lin.)

The authors are with University of California, Berkeley, Berkeley, CA 94720 USA (e-mail: linsenthu@gmail.com; smoazeni@berkeley.edu; ktset@berkeley.edu; vlada@berkeley.edu).

Color versions of one or more of the figures in this paper are available online at <http://ieeexplore.ieee.org>.

Digital Object Identifier 10.1109/JLT.2017.2757945

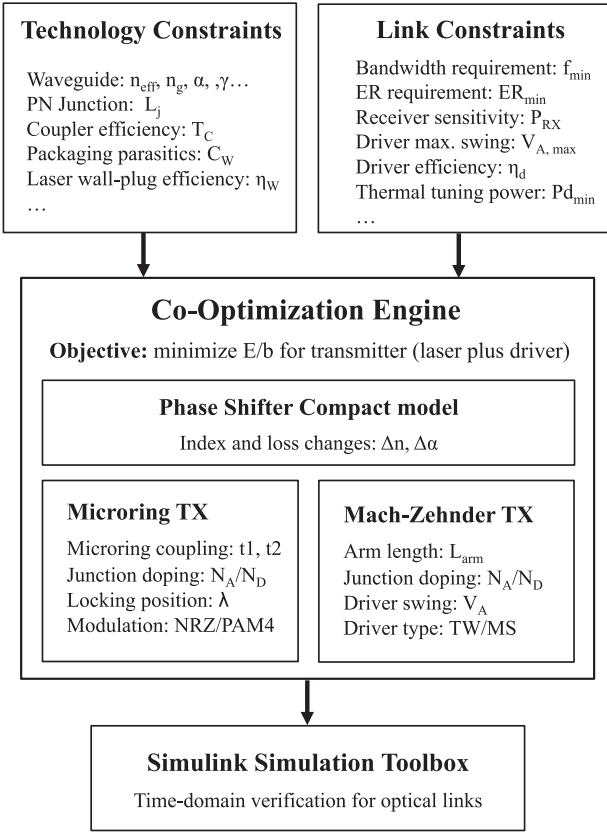


Fig. 1. The flowchart of the co-optimization framework for silicon photonic transmitters. The denotations here are used in derivations in the paper.

best energy efficiency. A new Simulink toolbox is introduced to capture dynamic behaviors of MRMs. This general-purpose toolbox can be used for simulating other optical systems as well. In addition, an MRM-based PAM4 transmitter is analyzed as a potential way to mitigate optical bandwidth constraints. In Section V, a co-optimization of the Mach-Zehnder transmitter is carried out for both multi-stage (MS) and traveling-wave (TW) drivers. Finally, a comparison between optimized MRM-based TX and optimized MZM-based TX given the same technology constraints is discussed in Section VI. Section VII concludes the paper.

## II. OVERVIEW OF CO-OPTIMIZATION FRAMEWORK

The objectives of the proposed framework are to lay the foundation for silicon photonic device and link co-design and to be readily applicable to a multitude of silicon photonic platforms. This framework is called “co-optimization” as it optimizes photonic device parameters such as doping levels and geometries alongside CMOS circuits and architectural choices. The optimization goal is to minimize the overall energy-per-bit (E/b) of the transmitter macro (laser plus driver) under both technology and link design constraints. The detailed constraints, as well as the overview of optimization framework, are shown in Fig. 1.

Challenges for designing a comprehensive, yet general, co-optimization framework stem mainly from three important criteria. First, the framework needs to be specific enough to

capture the intricacies of technology-dependent photonic device physics, without necessarily overburdening the optimizer. Second, the model needs to be generic enough to characterize the common waveguide and junction designs across many silicon photonic platforms. Third, it needs to consider key link constraints and provide a link-level picture that includes the transmitter, receiver and laser. Previous literature on link-level analysis and modeling of silicon photonic transmitters [21]–[23] often treats the optical devices as black boxes and do not consider doping and device design parameters altogether. For example, the critical trade-off between phase shift and optical loss under process constraints is often neglected. Other literature focusing on photonic device modeling [23]–[27] often relies on analytical expressions of optical mode distribution in the waveguide and can be too complex and cumbersome for link-level analysis. To overcome these issues, we model the silicon photonic modulators based on a simple yet accurate compact model for phase shifters. The paper focuses on depletion-mode pn-junction-based phase shifters, as they are widely used for high-speed modulators on different silicon photonic platforms [1]–[8]. This compact model incorporates waveguide geometry, mode confinement factor, and PN junction doping, all with some reasonable approximations. The compact model fits well with experimental results in various silicon photonic platforms.

As shown in Fig. 1, the co-optimization engine uses both technology and link constraints. The technology constraints are related to the photonic processes and includes parameters for waveguides, junctions, couplers and lasers. The link constraints are determined by the overall link budget and specific transceiver circuits. The engine optimizes microring and Mach-Zehnder transmitters separately based on the same phase shifter model with the goal of minimizing total E/b for laser and electronic driver combined. An optical simulation toolbox is developed in Simulink to verify the large-signal time-domain performance of the co-optimized transmitters. The optimizer is implemented in Matlab and can be integrated seamlessly with Simulink. Although this paper focuses on the transmitter side, the simulation toolbox can be applied to full optical links as well along with other communication toolboxes. This Simulink optical simulation toolbox is available online [35].

## III. PN-JUNCTION-BASED OPTICAL PHASE SHIFTER

### A. Compact Model of Optical Phase Shifter

The common building block for both MRM’s and MZM’s is the high-speed optical phase shifter. More specifically, this phase shift allows the constructive or destructive interference of light exiting the transmit waveguide, thereby creating a modulated output optical signal.

Due to the lack of Pockels effect, silicon photonic phase shifters rely on the carrier plasma dispersion effect. High-speed phase modulation is achieved with depletion-mode PN junctions. Within PN junctions, the number of excess electrons and holes strongly dictate the refractive index and absorption coefficient. Combined with the applied voltage across the junction, these factors affect the maximum phase shift as well as the loss. Device parameters for phase shifters include intrinsic index and

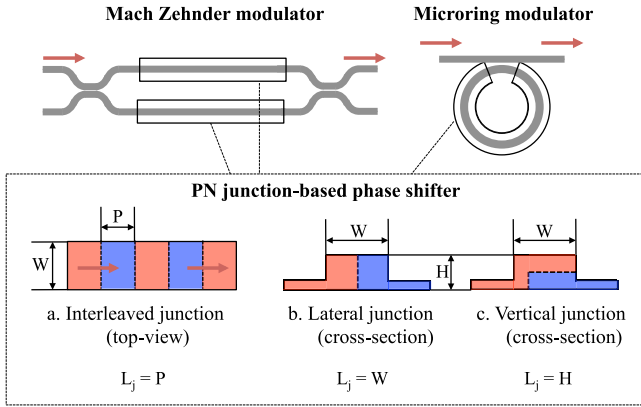


Fig. 2. Mach-Zehnder and microring modulators based on different PN junction phase shifters. Three common types of phase shifters are listed with top view or cross-section view. The corresponding feature lengths ( $L_j$ ) for these PN junctions are listed as well.

absorption, junction geometries and doping concentrations. The foundries often provide a wide range of doping concentrations by default and can potentially tune the doping levels for customers. Therefore, doping level is considered a key parameter in our optimization framework. There are three main types of junction designs as shown in Fig. 2. In this section, we propose a simplified phase shifter model that is applicable to most junction shapes.

The carrier plasma dispersion effect in crystalline silicon was first shown in [30]. The wavelength-dependent expressions for the material properties were commonly used with fitting parameters. According to the models in [28], both index and absorption vary as wavelength  $\lambda$  (m). The changes in refractive index  $n(\lambda)$  and absorption  $\alpha(\lambda)$  are given by:

$$\Delta n(\lambda) = -A\lambda^2 \Delta N - B\lambda^2 \Delta P^{0.8} \quad (1)$$

$$\Delta \alpha(\lambda) = C\lambda^2 \Delta N + D\lambda^2 \Delta P \text{ (cm}^{-1}\text{)}, \quad (2)$$

where  $\Delta N$  and  $\Delta P$  are changes in electron and hole concentrations ( $\text{cm}^{-3}$ ). The fitting parameters are  $A = 3.64 \times 10^{-10}$ ,  $B = 3.51 \times 10^{-6}$ ,  $C = 3.52 \times 10^{-6}$  and  $D = 2.4 \times 10^{-6}$ . Throughout the paper, power absorption coefficient is denoted by  $\alpha$ , and field absorption coefficient is denoted by  $\alpha_f$ , where  $\alpha = 2\alpha_f$ . The effective refractive index and absorption coefficient for an intrinsic silicon waveguide are denoted by  $n_{\text{eff},i}$  and  $\alpha_i$  respectively. The impacts of junction doping and external bias voltages can be derived in two steps. As the first step, a doped silicon waveguide without depletion region is assumed. For simplicity, the waveguide is assumed to be split evenly between uniform n-doping and uniform p-doping. The intermediate effective index  $n_{\text{eff},d}$  and absorption  $\alpha_d$  for a doped waveguide can be thereby approximated as

$$n_{\text{eff},d} \approx n_{\text{eff},i} - \gamma(A\lambda^2 N_D + B\lambda^2 N_A^{0.8})/2 \quad (3)$$

$$\alpha_d \approx \alpha_i + \gamma(C\lambda^2 N_D + D\lambda^2 N_A)/2. \quad (4)$$

where  $N_D$  and  $N_A$  are impurity densities for n-doping and p-doping respectively.  $\gamma$  represents the mode confinement factor for the waveguide ( $0 < \gamma < 1$ ). When optical mode is more

confined in the waveguide,  $\gamma$  increases and thus doping has a larger impact on optical properties.

In reality, depletion region always exists in the PN junction of a depletion-mode phase shifter. As the second step, we assume that bias voltage  $V$  is applied on the junction ( $V = 0$  when there is no external bias). The voltage-dependent effective refractive index and absorption coefficient are derived as

$$n_{\text{eff}}(V) \approx n_{\text{eff},d} + \frac{\gamma}{L_j} (A\lambda^2 N_D x_n(V) + B\lambda^2 N_A^{0.8} x_p(V)) \quad (5)$$

$$\alpha(V) \approx \alpha_d - \frac{\gamma}{L_j} (C\lambda^2 N_D x_n(V) + D\lambda^2 N_A x_p(V)) \quad (6)$$

where  $x_n(V)$  and  $x_p(V)$  are depletion widths on the n-doping and p-doping side of the PN junction. They are calculated by the set of equations below:

$$x_n(V) = \sqrt{\frac{2\epsilon N_A (V_{bi} - V)}{q N_D (N_A + N_D)}} \quad (7)$$

$$x_p(V) = \sqrt{\frac{2\epsilon N_D (V_{bi} - V)}{q N_A (N_A + N_D)}} \quad (8)$$

$$V_{bi} = \frac{k_B T}{q} \ln \frac{N_A N_D}{n_i^2}. \quad (9)$$

$L_j$  is defined as a feature length for PN junction. It is determined by the waveguide geometries and junction shapes. For different junction shapes, different feature lengths  $L_j$  are listed in Fig. 2. Intuitively, reducing  $L_j$  would improve phase modulation efficiency as the depletion region takes up a larger portion within the waveguide. For lateral and vertical junctions, feature length  $L_j$  are correlated with the confinement factor  $\gamma$ . For interleaved junctions, they are independent parameters. In general, reducing  $L_j/\gamma$  improves the overlap between the confined optical mode and depletion region and thereby improves phase modulation efficiency (5).

This model assumes that the perturbations in effective refractive index and absorption coefficient vary linearly as depletion width. This is an accurate assumption for interleaved junctions, and is a simplified first-order approximation for other junction designs with typical waveguide geometries. For lateral and vertical junctions, the model assumes uniform distribution of optical power in the waveguide.

## B. Model Verification on Different Platforms

Next the phase shifter model is applied to various silicon photonic platforms developed by multiple foundries. The model is verified against measurement data. Modulation efficiency  $V\pi L\pi$  is generally used for characterizing phase shifter performance, which is defined as the product of the required voltage swing ( $V_\pi$ ) and phase shifter length ( $L_\pi$ ) for  $\pi$  phase shift. For a voltage swing from 0 to  $V$ , the product is given by

$$V_\pi L_\pi = \frac{\lambda V}{2(n_{\text{eff}}(V) - n_{\text{eff}}(0))} \quad (10)$$



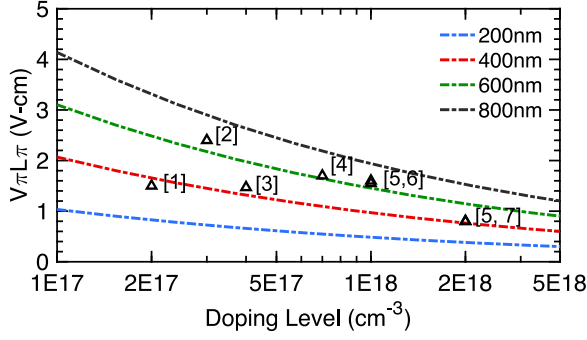


Fig. 3. Modulation efficiency  $V\pi L\pi$  vs. junction doping level. Dashed lines are predicted  $V\pi L\pi$  at  $-1$  V reverse bias when  $L_j/\gamma$  equals 200 nm, 400 nm, 600 nm and 800 nm. Reported data on various silicon photonic platforms [1]–[7] are marked here. Average concentration of n-type and p-type doping is used.

TABLE I  
MODELED PHASE SHIFTERS ON VARIOUS SI PHOTONIC PLATFORMS

Ref	Junction Type	Fab/Group	Doping (cm <sup>-3</sup> )	Width (nm)	Height (nm)	L <sub>j</sub> (nm)	Calculated $\gamma$
[1]	Interleaved	SMIC	2E17	450	340	300	0.83
[2]	Lateral	LETI	3E17	400	220	400	0.60
[3]	Interleaved	IBM	4E17	500	135	300	0.62
[4]	Lateral	IME	6E17	500	220	500	0.72
[5]	Lateral	IMEC	1E18	500	220	500	0.76
[5]	Interleaved	IMEC	2E18	500	220	300	0.72
[6]	Lateral	Oracle	1E18	480	300	480	0.85
[7]	Interleaved	IBM	2E18	500	170	280	0.67

The relationship between  $V\pi L\pi$  and doping levels for different  $L_j/\gamma$  is plotted in Fig. 3. The reported data points from multiple silicon photonic processes are marked in the same figure. All the measurement data are taken at around 1550 nm for consistency. This figure shows the distribution of doping levels in today's silicon photonic platforms and their corresponding  $V\pi L\pi$ . In addition, it can be used to estimate the waveguide and junction defined factor  $L_j/\gamma$  for these platforms.

More details about these waveguides and phase shifters are summarized in Table I. Only phase shifters based on lateral and interleaved junctions are included here due to insufficient measurement data for vertical junctions. Based on our proposed compact models, the mode confinement  $\gamma$  can be directly calculated from the measured  $V\pi L\pi$ . It is clear from the calculated results that  $\gamma$  decreases as the dimensions of the waveguide cross section shrinks because the optical mode is less confined. The typical value for  $\gamma$  is between 0.60 to 0.85. In our optimization framework,  $\gamma$  is assumed to be fixed and considered as a technology constraint. In Fig. 4, the voltage-dependency of  $V\pi L\pi$  predicted by the model are compared with the reported measurement data from three different silicon photonic platforms [4], [5], [7]. Among them, two use lateral junctions and one uses interleaved junction. Note that for these three phase shifters,  $L_j$  and  $\gamma$  are the same as their corresponding values listed in the table. The predicted modulation efficiencies matches well with measurement data.

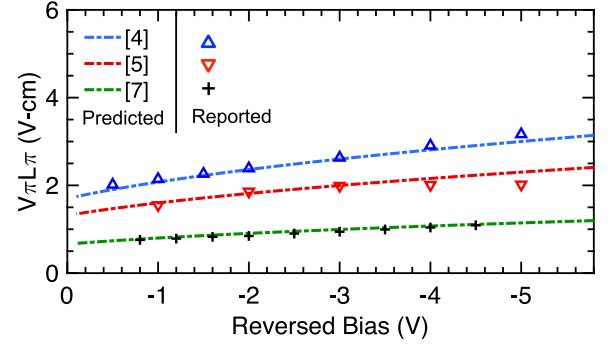


Fig. 4. Modulation efficiency  $V\pi L\pi$  vs. reversed bias voltage for phase shifters on three different platforms [4], [5], [7]. Detailed information are included in Table I. Note that [5] refers to the interleaved phase shifter on that platform.

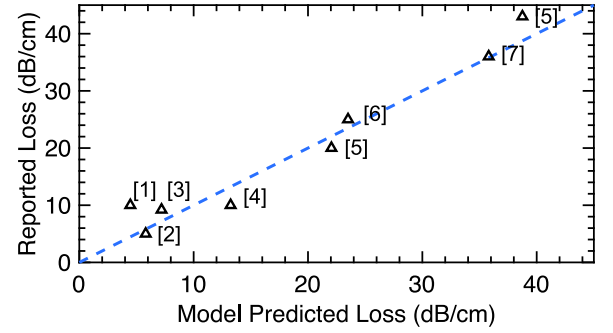


Fig. 5. Reported waveguide loss vs. predicted waveguide loss. The references for each data points are labeled in the figure [1]–[7].

For higher doping levels, modulation efficiency of the phase shifter improves at the cost of larger optical losses. This inherent trade-off is critical for doping optimization for MRM and MZM devices. The optical losses of the phase shifters, as calculated from 6, match well with measured waveguide losses from various platforms in Fig. 5. Overall, the proposed model considers junction design and mode confinement, captures the fundamental device trade-off between loss and phase shift, and fits accurately the voltage dependency on these optical properties. Although the model can be extended to include more physics details for specific designs such as junction asymmetry or actual mode profiles, it is efficient and accurate enough for this paper's system-level optimization.

#### IV. OPTIMIZATION OF MICRORING-BASED TRANSMITTER

##### A. Static Model of Microring Modulator

A microring modulator (MRM) typically consists of a silicon microring and three waveguide ports – input, output and drop ports, as shown in Fig. 6. The microring has a very small footprint compared to other modulators, with diameters as small as 10  $\mu\text{m}$ . This enables very low power modulation at sub-100 fJ/b driver energy due to its small device capacitance [8]. The microring itself is a pn-junction-based phase shifter that is driven by voltage drivers. The optical power at the output port of the ring changes as the round-trip phase is modulated by the driver.

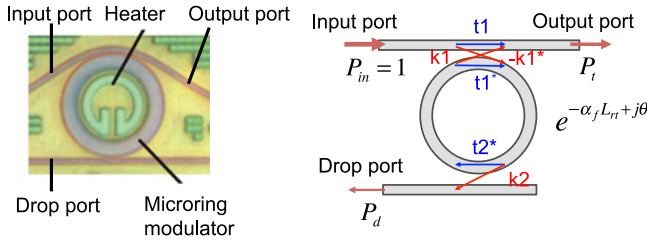


Fig. 6. Micrograph of microring modulator in zero-change 45 nm SOI process [8]. Model diagram of a microring modulator with drop port, where coupler and propagation coefficients for electric fields are labeled.

High-speed operation has been demonstrated with depletion-mode phase shifters [12], [18].

Microring modulators can be sensitive to temperature variations. For any practical system, the microring resonance needs to be adaptively locked to the laser wavelength through a **thermal tuning feedback loop**. Robust and efficient thermal tuning for microring modulators has been demonstrated with a running processor on the same chip [8]. As the sensing part of feedback loop, **a drop port waveguide is coupled to the microring to provide a port for monitoring the optical power level inside the cavity** (see Fig. 6). The feedback loop can be **closed with an embedded heater inside the microring for tuning the temperature**. More details about thermal tuning feedback designs and algorithms are shown in [21].

To optimize the modulator performance, we begin with the introduction of the static model of MRM's which relies on the phase shifter model in Section III. **The static model of the microring is derived based on the transfer matrix method (TMM)**, where the coupling between input/drop waveguides and the ring is represented by transfer matrices [31]. As shown in Fig. 6, the key device parameters for a microring include effective index  $n_{\text{eff}}$ , group index  $n_g$ , round-trip length  $L_{rt}$ , input coupler field transmission  $t_1$  and drop coupler field transmission  $t_2$ . Assuming a lossless coupler, we have  $|k_i|^2 + |t_i|^2 = 1$ , ( $i = 1, 2$ ), where  $k_1$  and  $k_2$  are cross-coupling coefficients. These coupler coefficients depend on the gap between the waveguide and microring cavity and can be determined through FDTD simulation. According to the TMM, the optical power at the output port  $P_t$  and drop port  $P_d$  can be derived as follows:

$$P_t = \left| \frac{t_1 - t_2 e^{-\alpha_f L_{rt} + i\theta}}{1 - t_1 t_2 e^{-\alpha_f L_{rt} + i\theta}} \right|^2 \quad (11)$$

$$P_d = \left| \frac{k_1^* k_2 e^{(-\alpha_f L_{rt} + i\theta)/2}}{1 - t_1 t_2 e^{-\alpha_f L_{rt} + i\theta}} \right|^2 \quad (12)$$

where  $\alpha_f$  is the field absorption coefficient and  $\theta$  is round-trip phase shift in the ring:  $\theta = 2\pi L_{rt} n_{\text{eff}} / \lambda$ . Note that  **$\alpha_f$  and  $n_{\text{eff}}$  are functions of bias voltage  $V$  and are dependent on doping and phase shifter designs**, which are given by the phase shifter compact model in Section III. As a result,  $P_t$  and  $P_d$  are functions of bias voltage  $V$  as well.

Assuming the bias voltage for 0 and 1 levels are  $V_0$  and  $V_1$  respectively, the normalized optical modulation amplitude

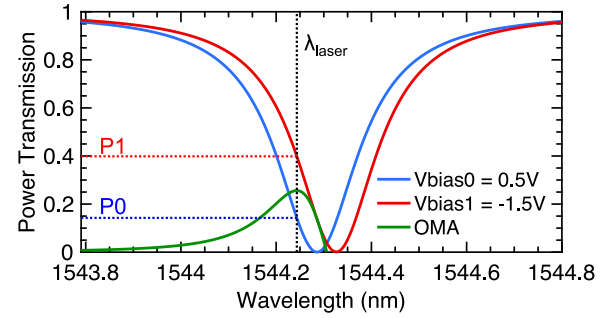


Fig. 7. Modeled power transmission spectra of microring modulator under two different bias voltages. Optimal laser wavelength to maximize OMA is labeled. For phase shifter model, we assumed that  $N_A = N_D = 10^{18} \text{ cm}^{-3}$ ,  $L_j = 500 \text{ nm}$  and  $\gamma = 0.75$ . The Q factor of this microring modulator is 7700. FSR of this microring is around 20 nm.

(OMA) with  $P_{in} = 1$  is given by

$$\text{OMA} = P_1 - P_0 = P_t(V_1) - P_t(V_0). \quad (13)$$

**Throughout the paper, OMA will be used to refer to the normalized optical modulation amplitude (or modulation depth).** The power transmission spectra of a typical microring modulator is shown in Fig. 7. At two different biases, the transfer functions of the microring have the same Lorentzian shape but different resonance wavelengths. The corresponding OMA can be calculated. The optimal laser wavelength that maximizes OMA is shown in the figure with optical powers for bit 1 and bit 0 labeled by  $P_1$  and  $P_0$  respectively. In the optimization framework, **the laser wavelength is considered an optimization parameter in order to maximize OMA**. In reality, the optimal laser detuning is in fact achieved by tuning the resonance wavelength of the microring with respect to the relatively stable laser wavelength. A robust data-independent tuning scheme with this function has been demonstrated [21]. **The resonance wavelength of the ring needs to be larger than the laser wavelength to achieve thermal stability under self-heating.**

The round-trip length of the microring,  $L_{rt}$ , is assumed to be  $30 \mu\text{m}$ . The size of the microring is chosen such that it provides a reasonably wide free spectral range (FSR) to enable WDM applications while also having a reasonably small bending loss. With a radius of around  $5 \mu\text{m}$ , the round-trip bending loss of an intrinsic silicon microring is only about 0.04 dB, which corresponds to 13 dB/cm for  $\alpha_i$  in 6. This includes scattering loss, radiative loss, and mode mismatch loss in the intrinsic microring. Optical properties of a typical silicon waveguide at 1550 nm are used in the analysis, where group index  $n_g = 3.89$  and wavelength-dependent effective index  $n_{\text{eff}}(\lambda) = 2.57 - 0.85(\lambda - 1.55)$  [28]. **These values for  $n_{\text{eff}}$ ,  $n_g$  and  $L_{rt}$  are used throughout the paper unless stated otherwise.**

## B. Transient Simulation in Simulink

The fundamental trade-off between OMA and optical bandwidth is the most critical challenge for high-speed modulation of microring modulators. Modeling dynamic behaviors of microrings accurately is the key for designing optical transmitters,

especially at very high data rate such as 50 Gb/s. According to coupled mode theory (CMT), the electrical-to-optical modulation bandwidth of microrings should be **inversely proportional to the photon lifetime  $\tau_p$  inside the cavity** [19], [20]. In addition, analytic small-signal model has revealed that **the small-signal bandwidth depends not only on the photon lifetime but also the detuning of the laser (frequency offset between laser and microring resonance)** [27]. However, **the more accurate modulation bandwidth for microring modulators has to be estimated through large-signal transient simulations.**

The photon lifetime  $\tau_p$  can be calculated from  $\tau_p = Q/\omega_0$ .  $\omega_0$  is the resonance frequency, and  $Q$  factor is defined as the time averaged stored energy per optical cycle divided by the total power loss. The stored energy in the ring is given by  $P_c L_{rt}/v_g$  with the group velocity  $v_g$  and the power flow in the cavity  $P_c$  [20]. In our case, the total power loss in the cavity stems from the input port coupling, drop port coupling and round-trip loss. Therefore, the  $Q$  factor is derived as

$$Q = \omega_0 \frac{P_c L_{rt}/v_g}{P_c (|k_1|^2 + |k_2|^2 + 1 - e^{-\alpha L_{rt}})} \quad (14)$$

$$\approx \frac{\omega_0 n_g L_{rt}}{c (|k_1|^2 + |k_2|^2 + \alpha L_{rt})}$$

with the speed of light  $c$  and group index  $n_g$ . The round-trip loss is assumed to be small in the approximation above. Now the photon lifetime  $\tau_p$  in the microring cavity is given by

$$\tau_p = \frac{Q}{\omega_0} = \frac{n_g L_{rt}}{c (|k_1|^2 + |k_2|^2 + \alpha L_{rt})} \quad (15)$$

The optical bandwidth or the corresponding full-width-at-half-maximum (FWHM) bandwidth can be calculated as

$$f_{\text{optical}} = \frac{1}{2\pi\tau_p} \quad (16)$$

**The actual modulation bandwidth  $f_{3dB}$  of the MRM is proportional to the optical bandwidth  $f_{\text{optical}}$**  [19]. Large-signal simulation is needed to estimate the ratio more accurately given the optimized microring design and laser detuning.

An open-source Simulink toolbox is developed for simulating silicon photonic devices and systems [35]. The toolbox contains a library of the basic optical elements such as lasers, waveguides, phase shifters and couplers. Complex photonic devices are constructed with these basic building blocks. **The basic theory behind Simulink simulation is the same as the previous Verilog-A co-simulation framework** [29]. One of the major differences is that the new toolbox adopts the proposed phase shifter model in Section III, which allows more physical details to be included. The Simulink toolbox works seamlessly with the **co-optimization framework** developed in MATLAB.

The Simulink schematic of a microring-based optical link is shown in Fig. 8. It consists of two  $2 \times 2$  couplers for input and drop ports and two **phase shifters with half the round-trip length**. The phase shifter blocks compute the phase shift and optical loss using the proposed compact model. Within the phase shifter block, **a built-in delay function is used to generate the propagation delay of the optical signal in the waveguide.**

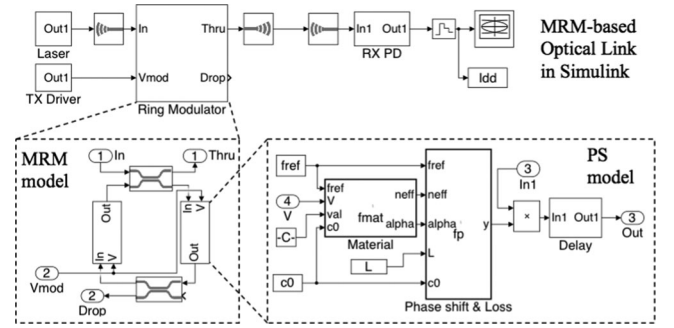


Fig. 8. Schematic of MRM-based optical link in Simulink and the close-ups of microring modulator (MRM) block and the phase shifter (PS) block.

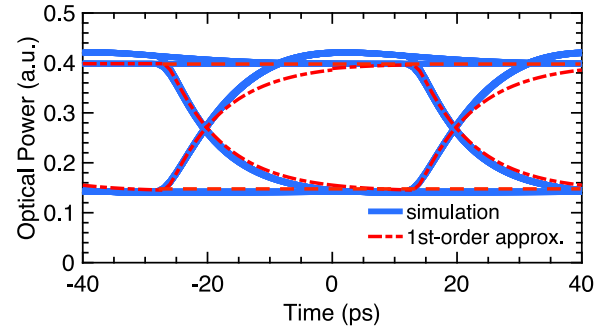


Fig. 9. Simulated eye diagram at 25 Gb/s. Device parameters are the same as the microring in Fig. 7 with optical bandwidth of around 25 GHz. Laser detuning is set to optimize OMA. A first-order low-pass filter approximation with 3 dB bandwidth of 20 GHz is represented with red dashed line.

As an example, the microring modulator in Fig. 7 is simulated using this work's Simulink toolbox. A 25 Gb/s eye diagram is shown in Fig. 9. In this transient simulation, the driver signal swings between 0.5 V and  $-1.5$  V with ideal, sharp transitions. Therefore, the eye diagram is solely governed by the optical dynamic behavior of the microring modulator. It is interesting that **the rising transition of the eye is faster than the falling transition and even causes a slight overshoot**. This is consistent with the small-signal analysis [27] **where larger laser detuning corresponds to larger small-signal bandwidth**. **The asymmetry in the eye diagram should be balanced by adjusting driver strength for pulling up and pulling down.**

In our optimization engine, **the modulation bandwidth is assumed to be limited by the slower falling edge**. A first-order low-pass filter with a 3 dB bandwidth  $f_{3dB}$  is used in Simulink to approximate the modulation bandwidth. The simulation results show  $f_{3dB} \approx 0.8 f_{\text{optical}}$  for the microring in Fig. 9. In our optimization,  $f_{3dB}$  is chosen to be at least  $0.8/T_b$  to ensure ISI-free modulation at a data rate of  $1/T_b$  according to the eye diagram. Therefore, **the optical bandwidth constraint for a microring modulator in the optimization can be simply given by**

$$f_{\text{optical}} \geq \frac{1}{T_b}. \quad (17)$$

For a 50 Gb/s MRM, the optical bandwidth constraint is thereby set to 50 GHz with the actual electrical-to-optical modulation bandwidth being around 40 GHz. Transient simulations will be



used to further verify the dynamic performance for 50 Gb/s optimized microring transmitters.

### C. Optimization of Microring Modulator Design

For a typical MRM-based transmitter, laser power dominates the total power consumption of the transmitter macro as the driver power is usually much lower. Therefore, minimizing the overall E/b for the transmitter (driver plus laser) is equivalent to maximizing the normalized OMA of the microring modulator.

For analysis purposes, we choose to use a typical feature length  $L_j$  (500 nm) and a typical mode confinement factor  $\gamma$  (0.75) for phase shifters in this paper. These numbers are within the range of parameters on the typical silicon photonic platforms summarized in Table I. The other fixed parameters for our MRM analysis include round-trip length of the ring and waveguide intrinsic loss, which are set to be 30  $\mu\text{m}$  and 13 dB/cm [28] respectively. These preset constraints largely depend on the photonic platform and targeted link application. However, the insights and trends discovered through the framework are useful over a wide range of technology and link constraints.

For each doping level for the PN junction ( $N_A$  and  $N_D$ ), the optimizer would find the optimal coupling coefficients at input and drop ports ( $t_1$  and  $t_2$ ) and the optimal laser detuning  $\Delta\lambda$  for thermal locking, with the goal being to maximize the normalized OMA. For simplicity, symmetric pn doping is assumed with  $N_A = N_D$ . The driver swing is assumed to be from 0.5 V to  $-1.5$  V. The optimization is subject to the following constraints:

- 1) Optical bandwidth requirement:

$$f_{\text{optical}} \geq f_{\text{min}}. \quad (18)$$

- 2) Extinction ratio (ER) requirement:

$$\text{ER} = \frac{P_t(V_1)}{P_t(V_0)} \geq \text{ER}_{\text{min}} \quad (19)$$

- 3) Enough average drop port power for thermal tuning:

$$\frac{P_d(V_1) + P_d(V_0)}{2} \geq P_{d,\text{min}}. \quad (20)$$

The extinction ratio requirement  $\text{ER}_{\text{min}}$  is set to 3.5 dB according to 100G PSM4 and CWDM4 technical specifications [36], [37]. Drop port power  $P_{d,\text{min}}$  is set to be  $0.01 P_{\text{in}}$  in order to achieve accurate power monitoring and thermal tuning based on the required drop port current in [8]. Optimizations are carried out for different doping levels for the PN junction. The optimal OMAs are shown in Fig. 10 for three targeted NRZ datarates (25, 35, 50 Gb/s). The corresponding optical bandwidths (25, 35, 50 GHz) are used in the optimization engine based on the large-signal transient simulation in this paper.

According to Fig. 10, an optimal doping level exists for each bandwidth requirement. Intuitively, increasing doping could improve the modulation efficiency of the phase shifter and could improve OMA. However, as we increase doping levels, the excessive optical loss in the ring might eventually lower the Q factor and degrade the OMA. Therefore, it is critical to find the optimal doping levels. It is important that the optimal doping level increases as the required optical bandwidth increases. The optimal doping for achieving 50 GHz optical bandwidth is

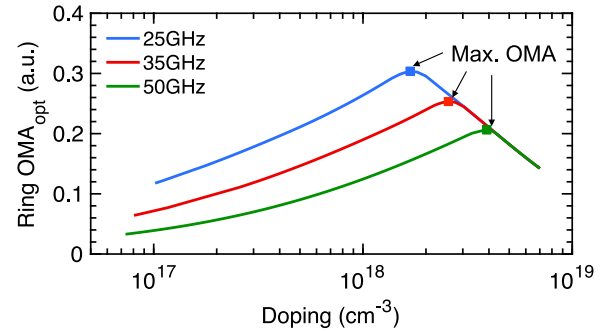


Fig. 10. Optimized OMA for  $f_{\text{optical}}$  25 GHz, 35 GHz and 50 GHz versus doping levels in the PN junction. Bias conditions are  $V_0 = 0.5$  V and  $V_1 = -1.5$  V. Technology constraints: PN junction feature length  $L_j = 500$  nm and optical mode confinement factor  $\gamma = 0.75$ .  $L_{rt} = 30$   $\mu\text{m}$ , intrinsic loss 13 dB/cm [28]. Symmetric pn-junctions are assumed for simplicity.

around  $3.8 \times 10^{18} \text{ cm}^{-3}$ . This doping level is in fact close to that used in the 56 Gb/s microring modulator reported so far [12].

The corresponding device parameters given by the optimization engine are shown in Fig. 11, including Q factor, extinction ratio (ER), insertion loss (IL), coupler coefficients ( $t_1$  and  $t_2$ ) and the microring coupling factor ( $\beta$ ). Here we define microring coupling factor  $\beta$  as  $\beta = t_1 e^{\alpha_f L} / t_2$  to represent the coupling status of microrings. When  $\beta < 1$ , the microring is over coupled; when  $\beta = 1$ , it is critically coupled; when  $\beta > 1$ , the microring is under coupled. These parameters can be used as a design reference or provide in-depth insights for microring design.

For Fig. 11(a)–(f), we define three different doping regions to get more insights into the microring optimization. The 25 GHz microring is used as an example. Region A is the coupling-limited region where doping levels are relatively low. Q factor is effectively controlled by the coupler designs assuming fixed ring circumference and negligible round trip ring loss. Drop port coupling should be used to match the input port coupling. By doing so, the microring can be brought closer to critical coupling ( $\beta = 1$ ) to improve OMA. Region C is the loss-limited region where doping levels are relatively high. The Q factor drops below the targeted value as it is dictated by the excessive doping loss. Interestingly,  $t_1$  has to decrease to prevent the microring from getting too under coupled and breaking the ER constraint. All the microrings eventually get limited by the ER constraint as doping increases.

The optimal design with the maximum OMA is achieved in region B, where doping levels are between the regions A and C. For the optimal designs, input coupling is well balanced with the optical loss inside the cavity resulting in minimum drop port coupling. The microrings are slightly under-coupled. In this region, input coupling decreases as doping increase in order to maintain constant Q factor. If the available doping levels are not in region B, different optimization strategies are needed according to the analysis above.

### D. Microring-Based NRZ Transmitter Design

The driver circuit is modeled as shown in Fig. 12. It consists of a high-speed serializer, pre-drivers and a final driver stage. The

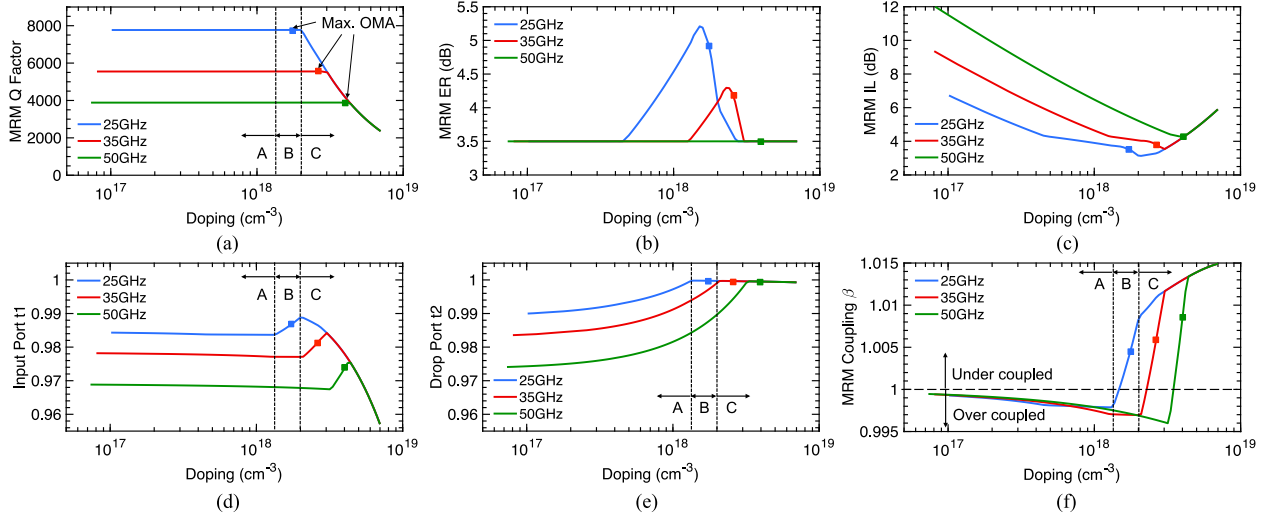


Fig. 11. Key characteristics of the optimal microring designs for different doping levels with the design points corresponding to maximum OMAs labeled. The optimization constraints corresponds to the curves in the Fig. 10. Three operation regions (A-C) are labeled for 25 GHz operation as an example. A is coupling-limited region, C is loss-limited region and B is the optimal region. Note that  $t_1$  and  $t_2$  are transmission coefficients at the couplers. Stronger coupling means smaller  $t_1$  and  $t_2$ .

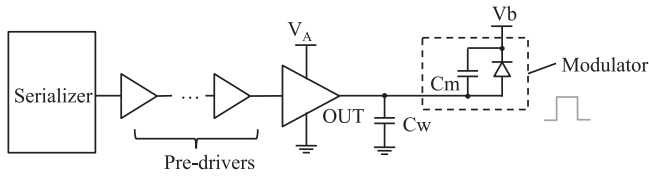


Fig. 12. Transmitter circuits for ring modulator.  $C_w$  is the wire and packaging parasitic capacitance, and  $C_m$  is the modulator junction capacitance.

final stage driver can be a simple **inverter** driving one electrode of the modulator in single-end fashion with voltage swing of  $V_{DD}$ . **Alternatively**, the final stage can be a high-swing driver or a pull-push driver, which can be implemented using stacked transistors and level shifters. **The typical swing for a high-speed high-swing driver is  $2V_{DD}$  and  $V_{DD}$  is 1V for standard CMOS processes.**

In our optimization, we assume the voltage swing  $V_A$  to be either 1 V or 2 V. With  $V_b$  applied on the **cathode**, the voltage bias on the PN junction swings between  $-V_b$  to  $V_A - V_b$ . In order to maintain depletion mode, the maximum forward  $V_A - V_b$  should be smaller than the **built-in voltage  $V_{bi}$** , which is **between 0.7 V to 1.1 V for the typical doping range from  $10^{16}$  to  $10^{19} \text{ cm}^{-3}$** . For simplicity, we always set  $V_A - V_b = 0.5 \text{ V}$  for all doping levels in the optimization engine. This is consistent with experimental settings for microrings on various platforms [8], [13]. **Microring performance might degrade due to the effect of free carrier absorption if the forward-bias voltage is further increased.** Under these conditions, the E/b for the driver circuits is given by

$$E_{dr} = \frac{1}{4\eta_d} V_A \int_{-V_b}^{V_A - V_b} (C_m(V) + C_w) dV. \quad (21)$$

where driver efficiency  $\eta_d$  is assumed to be 20% considering reasonable fan-out for pre-driver stages at 50 Gb/s.

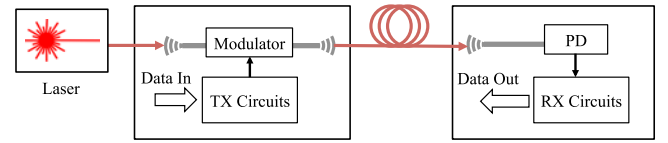


Fig. 13. Diagram of a full optical link with external laser source.

The capacitance density of the PN junction is given by

$$C_j(V) = \sqrt{\frac{q\epsilon N_A N_D}{2(V_{bi} - V)(N_A + N_D)}}. \quad (22)$$

The modulator capacitance depends on the type of the PN junctions. For lateral junctions,  $C_m \approx C_j(V)LH$ ; for interleaved junctions,  $C_m \approx C_j(V)L^2WH/P$ ; for vertical junctions,  $C_m \approx C_j(V)LW$ .  $H$ ,  $P$  and  $W$  are defined in Fig. 2 and  $L$  is the total length of the PN junction. In the case of microrings,  $L = L_{rt}$ . **With the typical device parameters,  $C_m$  ranges from 15 to 25 fF.** 文献

**The total wiring capacitance  $C_w$  ranges from 5 fF to 40 fF depending on the packaging type.** For 3D integration using copper pillars, the total wiring capacitance would be around 20 fF [11]. For 3D integration with through-oxide-vias (TOVs) or monolithic integration, the wiring parasitics can be reduced to 5–10 fF [8], [9]. In our analysis, we assumed  $C_w$  to be 20 fF. The energy consumption for modulator driver circuits can be calculated based on the equations above.

Even so, laser power dominates the total power for MRM transmitters. For a typical silicon photonic link in Fig. 13, the optical power gets attenuated by three fiber-to-chip optical couplers and the transmitter before it reaches the receiver-side photodetector. **The minimal OMA required at the receiver input to reach a certain BER target is defined as the receiver sensitivity, denoted by  $P_{RX}$  in this paper.** The total E/b consumed by the



TABLE II  
PARAMETERS FOR 50 GB/S SILICON PHOTONIC LINK BUDGETING

Sensitivity $P_{RX}$	Coupler $\alpha_c$	Margin $\eta_m$	Laser $\eta_w$
-10 dBm	3dB	3dB	10%

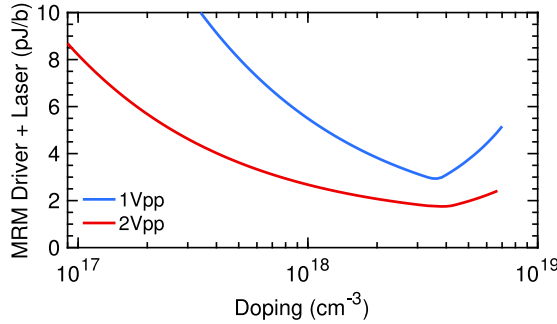


Fig. 14. Model-estimated total E/b for microring driver + laser for microring-based NRZ transmitter at 50 Gb/s. Two different driver swings are considered (1 V and 2 V). The microring is optimized for each doping levels, which corresponds to the designs in Figs. 10 and 11.

laser source is derived as

$$E_{laser} = \frac{P_{RX}}{\eta_m \cdot \eta_w \cdot \alpha_c^3 \cdot \text{OMA}_{\text{mod}} \cdot f_b} \quad (23)$$

where  $\eta_w$  is the wall-plug efficiency of the laser module,  $\alpha_c$  is optical coupler loss coefficient,  $f_b$  is the bit rate and  $\eta_m$  accounts for additional margin in the link budget.  $\text{OMA}_{\text{mod}}$  is the normalized OMA for the modulator. An optical receiver using 14 nm FinFET has achieved -10 dBm optical sensitivity at 50 Gb/s reaching  $10^{-12}$  BER [10]. We use the measurement data from this paper as a reference for receiver sensitivity throughout the paper such that the link constraints could reflect the state-of-the-art CMOS technology.

The total E/b for MRM-based transmitter is the sum of the driver circuit and laser power:

$$E_{tot} = E_{dr} + E_{laser}. \quad (24)$$

Typical numbers for parameters used in 23 are listed in Table II. Based on the results in Fig. 10, the energy-per-bit  $E_{tot}$  for the optimized 50 Gb/s MRM-based transmitters can be calculated. The relationship between optimized  $E_{tot}$  (laser plus driver power) and doping levels are shown in Fig. 14.

The results show that higher driver swing improves the overall energy efficiency for MRM transmitters as laser power dominates and higher swing improves OMA. The total transmitter power is not sensitive to the increased driver power due to higher swing. Therefore it makes sense to always choose high swing drivers if driver bandwidth allows. In addition, it is also critical to co-optimize the modulator design to maximize OMA as discussed before. The 50 Gb/s MRM-based NRZ transmitter with the optimized microring device and 2 V driver voltage swing consumes 1.7 pJ/b in total – 1.5 pJ/b by laser and only 0.2 pJ/b by driver circuits. More results and the optimal dopings can be found in Table III. Note that the above analysis is done assuming 3D hybrid integration between circuits and photonics. Switching to monolithic integration would yield even lower driver power

TABLE III  
50 GB/S MICRORING TX OPTIMAL DOPING AND POWER ( pJ/B)

	$V_A$ (V)	Doping ( $\text{cm}^{-3}$ )	Laser	Driver	Total
NRZ	1.0	$3.7 \times 10^{18}$	2.9	0.06	3.0
NRZ	2.0	$3.8 \times 10^{18}$	1.5	0.21	<b>1.7</b>
PAM4	1.0	$1.5 \times 10^{18}$	2.1	0.04	2.1
PAM4	2.0	$1.7 \times 10^{18}$	1.3	0.10	<b>1.4</b>

and thus further improve the energy efficiency of the transmitter and be even further dominated by laser power.

#### E. Microring-Based PAM4 Transmitter Design

As shown in Fig. 10, the microring modulator can achieve higher OMA at the cost of optical bandwidth. In other words, reducing bandwidth requirement means improving OMA and lowering laser power for MRM-based optical links. One potential way to relax the bandwidth constraint while maintaining the same data rate is to use PAM4 instead of conventional NRZ modulation, where the front-end bandwidth is halved in a PAM4 modulation scheme to attain the same bit rate. There has been analysis comparing the energy efficiency of microring-based PAM4 transmitters with NRZ transmitters [32]. In this paper, we use the proposed optimization framework to optimize microring designs for NRZ and PAM4 separately. The optimized microring-based PAM4 transmitter is then compared to the optimized NRZ transmitter at 50 Gb/s under the same process constraints. Transient simulations are also used to verify the transmitter performances. Note that practical design constraints outside the scope of this work would need to be taken into consideration as well to validate the benefits of PAM4 versus NRZ. This paper is intended to give a first-pass, fundamental comparison between the two schemes.

There are multiple ways to generate the PAM4 optical signal with silicon microring modulators. For the first approach, an electrical DAC is used to drive the microring modulator [33], [34]. This architecture is shown in Fig. 15(a). Due to nonlinearity of the electrical-to-optical response of microrings, a lookup table is required in order to pre-distort the drive signal and achieve symmetric PAM4 eyes. The second approach uses an optical DAC to generate the PAM4 signals instead of using an electrical DAC [18]. As shown in Fig. 15(b), the microring is segmented into  $2^N$  uniform segments to form an N-bit optical DAC. In this topology, the PAM4 data needs to be thermometer-coded, and each slice of driver connects to one segment in the microring. The segmentation can be directly implemented in microrings with interleaved PN junction [18]. For the third approach, the microring is segmented into only two segments – one LSB and one MSB with binary weights [33]. Each of two segments is driven by one driver and serializer as in Fig. 15(c).

Linearity is the key criterion for choosing microring-based PAM4 architectures, which can be evaluated with the static model in Section IV. The optical responses of a 4-bit electrical DAC and a 4-bit optical DAC are compared in Fig. 16(a). For the comparison, the total voltage swing of the electrical DAC equals that of the driver for each small segment in the optical

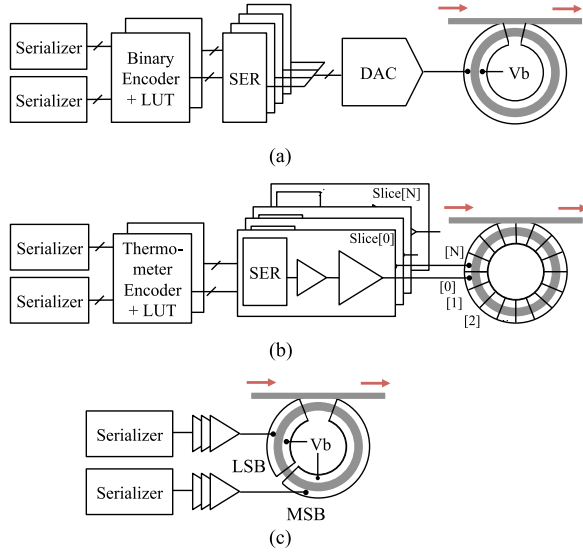


Fig. 15. Microring-based PAM4 Transmitters: (a) electrical DAC driver (b) optical DAC based on segmented microring (c) microring with two segments.

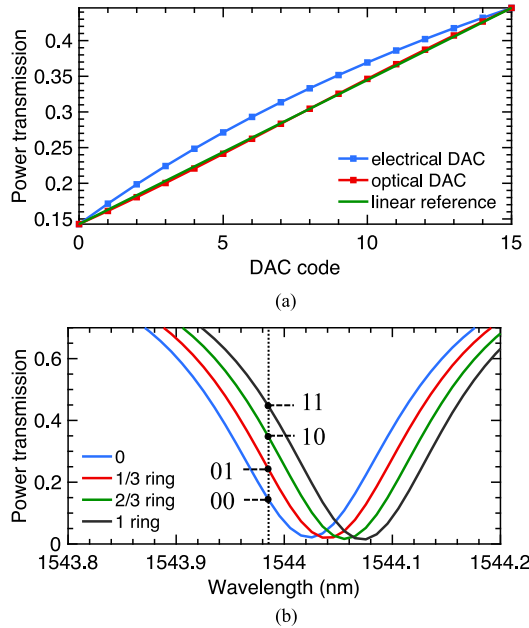


Fig. 16. (a) Linearity comparison between 5-bit electrical DAC and 5-bit optical DAC for MRM-based transmitter. (b) Transmission spectra for a microring with two binary weighted segments. The microring here has an optical bandwidth of 25 GHz.

DAC. The same optimized microring modulators are used with 25 GHz optical bandwidth and 50 Gb/s targeted data rate. For such microrings, **the optical response of the optical DAC is more linear compared to that of the electrical DAC**. It also shows that the **third architecture using two segments should offer sufficient linearity for generating the balanced PAM4 signals at 50 Gb/s**.

The second and third architectures should be chosen depending on whether programmability is required to handle process variations. Despite of the architecture difference, they are both based on the same operation principles. The common transfer functions are shown in Fig. 16 as different portion of the ring is reverse biased by the corresponding driver. The microring

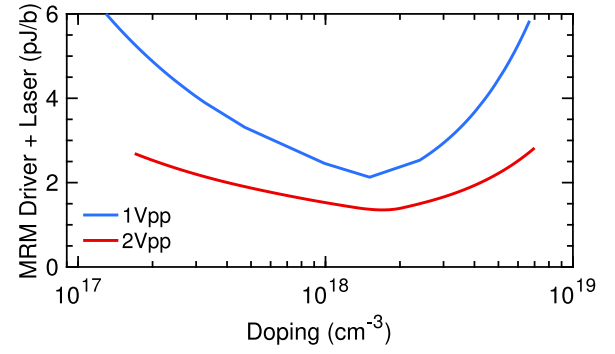


Fig. 17. Model estimated total E/b for microring driver+laser for microring-based PAM4 transmitter at 50 Gb/s. Two different driver swings are considered (1 V and 2 V). The microring is optimized for each doping levels, which corresponds to the designs in Figs. 10 and 11.

design and laser detuning are optimized for 50 Gb/s PAM4, and the four optical levels show very good linearity.

For 50 Gb/s PAM4, the optimization engine optimizes the OMA of a microring modulator with 25 GHz optical bandwidth, as shown in Fig. 10. A 25 Gb/s NRZ receiver could achieve a sensitivity of  $-14$  dBm according to [10]. **In our analysis, the required total eye height for 50 Gb/s PAM4 receiver is approximated as 3x single eye height for 25 Gb/s NRZ receiver, neglecting any other circuit overhead.** Therefore the new receiver sensitivity  $P_{RX}$  becomes  $-9.2$  dBm, and the new laser power  $E_{laser}$  can be calculated according to 23. For the new driver power  $E_{dr}$ , the wiring parasitics are now doubled for two-segment microrings as packaging capacitance doubles and still dominates  $C_w$ . The new expression for  $E_{dr}$  should be

$$E_{dr} = \frac{1}{2} \cdot \frac{1}{4\eta_d} V_A \int_{-V_b}^{V_A - V_b} (C_m(V) + 2C_w) dV \quad (25)$$

Now the total energy  $E_{tot}$  for driver and laser for microring-based PAM4 transmitter at 50 Gb/s can be calculated. The optimization results at two different bias voltages (1 V and 2 V) are shown in Fig. 17 assuming the same bias condition for  $V_b$  as the NRZ case. The optimal doping level and the best E/b for microring-based NRZ and PAM4 transmitters are compared in Table III. **The required Q for PAM4 microring modulator are doubled as optical bandwidth requirement is halved.** Therefore the optimal doping for PAM4 microring is less than that for NRZ microring. **From Table III, the optimal doping level for PAM4 microrings is only half of the optimal doping in the NRZ case.** Given the same technology and link constraints, microring-based PAM4 modulator can save nearly 20% total TX power compared to the NRZ modulator.

Transient simulations are carried out in order to verify the performance of 50 Gb/s microring NRZ and PAM4 transmitters. The device parameters for modulators in Simulink framework are set by the output of the optimization engine. The driver swings are assumed to be the same. The simulated eye diagrams are shown in Fig. 18. The modulators are optimized under the same technology and link constraints by the engine. The eye heights for PAM4 and NRZ in these two eye diagrams can be compared directly as the optical power is normalized. Total OMA height for PAM4 microring is increased by about 50% from NRZ microring. Detailed full link optimization

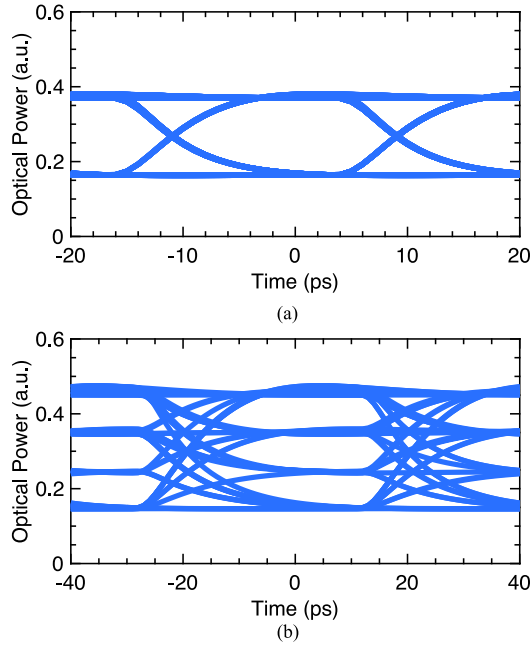


Fig. 18. Transient simulation of the 50 Gb/s MRM-based NRZ transmitter and PAM4 transmitter. The microrings are optimized in each case with the same process and link constraints. The optical power for y-axis is normalized to the input power for microrings.

including receiver circuits will be required to compare the full link power. For driver and laser portion, the potential power saving for PAM4 is around 20% at 50 Gb/s. Another observation is that microring PAM4 eye diagram is not balanced due to the asymmetry of the rise and fall time. Therefore, it is even more critical for PAM4 drivers to adjust pull-up and pull-down strengths compared with NRZ drivers. By doing so, the four signal levels in the optical PAM4 eye diagram can be well balanced.

## V. OPTIMIZATION OF MACH-ZEHNDER TRANSMITTER

### A. Overview of Mach-Zehnder Modulator

Mach-Zehnder modulators (MZM) have traditionally been used for optical communication due to its simple interferometric structure. A MZM consists of two balanced arms with embedded phase shifters. The output light intensity is modulated as a result of optical interference when phase shifts are introduced in the arms. On silicon photonic platforms, the phase shifters are normally made of PN junctions. The same set of technology constraints need to be applied. There are two major challenges for designing an energy efficient MZM. First, there is a trade-off between phase modulation efficiency and propagation loss for phase shifters. This would cause high insertion loss and low OMA for the MZM. Second, the device capacitance is much larger than microrings and the driver power could dominate the total power consumption. As a result, co-optimization of electrical driver and optical modulator is essential for designing low power MZM transmitters.

There are two basic architectures for MZM transmitter, one based on multi-stage drivers and one based on traveling-wave drivers, as shown in Fig. 19. For multi-stage MZM (MS-MZM),

the arms are segmented into multiple segments which are modulated individually by distributed voltage drivers. Delay units are inserted between these electrical drivers to match with the propagation velocity of optical signal inside the waveguide. For traveling-wave MZM (TW-MZM), the transmission lines are used as the electrodes. Delay matching is also required between optical waveguide and electrical transmission line. Traveling-wave drivers are typically more energy efficient than multi-stage drivers at high data rates [24]. Because the power of TW driver is independent of the device capacitance of MZM and gets amortized at high data rates. However TW-MZM may suffer from limited OMA due to lower voltage swing and high transmission line loss. Therefore, electronic-photonics co-optimization is needed to compare the overall energy efficiency of these two architectures,

The normalized transmitted power of both MZMs can be approximated as the following [24]:

$$P_t = e^{-\alpha L} \sin^2 \left( \frac{\Delta\phi}{2} \right) \quad (26)$$

where  $\alpha$  is the optical absorption coefficient,  $L$  is the length of each arm, and  $\Delta\phi$  is the phase difference between the two paths. Since the two arms of MZM are driven differentially,  $\Delta\phi$  equals  $\phi_0 + \Delta\phi_{mod}$  for bit "1" or  $\phi_0 - \Delta\phi_{mod}$  for bit "0".  $\phi_0$  is the static phase offset for adjusting OMA and ER.  $\Delta\phi_{mod}$  is the modulation phase shift introduced on each arm by the voltage drivers, which will be derived depending on the architecture choice. The same compact model for optical phase that is used for microring modulator will be reused for MS-MZM and TW-MZM in the proceeding sections.

### B. Multi-Stage Mach-Zehnder Transmitter

Since the same voltage swing is applied to each segment of the arm, the total modulation phase shift for one arm now becomes

$$\Delta\phi_{mod} = (2\pi L/\lambda) \cdot (n_{eff}(V_1) - n_{eff}(V_0)) \quad (27)$$

where  $V_1$  and  $V_0$  correspond to bias voltages for generating bit "1" and bit "0". The effective index  $n_{eff}$  and optical loss  $\alpha$  are governed by the phase shifter model. They are both functions of doping levels for the PN junction based phase shifter. In the optimization engine for MS-MZM, the power levels for bit 1 and bit 0 are calculated as

$$P_{t1} = e^{-\alpha L} \sin^2 \left( \frac{\phi_0 + \Delta\phi_{mod}}{2} \right) \quad (28)$$

$$P_{t0} = e^{-\alpha L} \sin^2 \left( \frac{\phi_0 - \Delta\phi_{mod}}{2} \right) \quad (29)$$

The normalized OMA and ER are given by

$$OMA = P_{t1} - P_{t0} \quad (30)$$

$$ER = P_{t1}/P_{t0} \quad (31)$$

The E/b for the laser  $E_{laser}$  can be calculated according to 23 similar to microring-based optical links. For the 50 Gb/s MZM link, the receiver sensitivity, couplers losses, link margin and laser wall-plug efficiency are assumed to be same as the 50 Gb/s microring-based NRZ link.

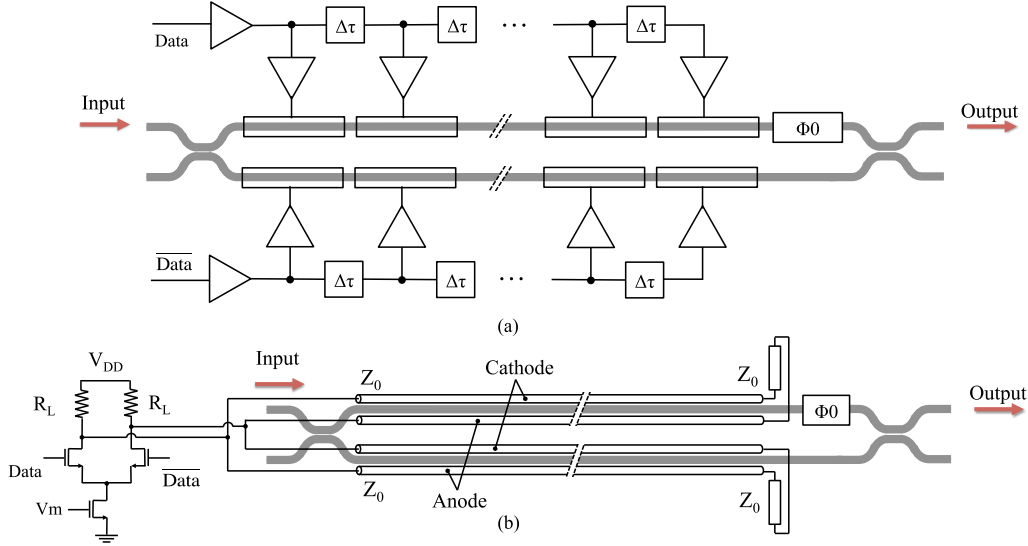


Fig. 19. (a) Architecture of Multi-stage Mach-Zehnder Modulator (MS-MZM) (b) Architecture of Traveling wave Mach-Zehnder Modulator (TW-MZM).

MS-MZM drivers are generally very **power hungry**. The total E/b for the modulator drivers is calculated as follows:

$$E_{dr,MS} = \frac{1}{4\eta_d} V_{dd} \int_{-V_{dd}}^0 (C_m(V) + C_w L) dV. \quad (32)$$

where driver efficiency  $\eta_d$  is set to 20%.  $C_w$  is set to 0.3 fF/ $\mu\text{m}$  assuming that the parasitic capacitance for the electrodes is 0.2 fF/ $\mu\text{m}$  and the amortized pad capacitance is 0.1 fF/ $\mu\text{m}$  [24]. Modulator capacitance  $C_m$  can be calculated the same way as microring modulators. The optimization engine for MZM assumes the same junction feature length  $L_j$  (500 nm) and mode confinement factor  $\gamma$  (0.75) for the waveguides as MRM. The intrinsic loss for the straight waveguide is set to 3 dB/cm [28]. We assume that the MZM drivers can be sufficiently sized to meet the bandwidth requirement for the target data rate regardless of doping levels and bias conditions.

The objective of the MZM optimization engine is to minimize total transmitter energy-per-bit E/b, including both laser wall-plug energy and TX driver energy. When the arms are driven differentially as in Fig. 19(a), the total transmitter energy for MS-MZM is given by

$$E_{TX,MS} = E_{laser} + 2E_{dr,MS} \quad (33)$$

For each doping level in the PN junction ( $N_A$  and  $N_D$ ), the optimization engine finds the optimal arm length  $L$  and static phase offset  $\phi_0$  to minimize the total E/b for the transmitter  $E_{TX,MS}$ . It is subject to the same ER constraint (3.5 dB) and the same receiver sensitivity (−10 dBm at 50 Gb/s) as MRM-based photonic links.

Co-optimization is carried out for MS-MZMs with two different driver voltages (1 V and 2 V) across the typical doping range. The total transmitter E/b, the laser power and the optimal arm length  $L_{opt}$  found by the optimization engine are shown in Fig. 20. Optimal doping levels exist for each voltage swing. Initially increasing the doping levels could improve the modulation efficiency and effectively improve the transmitter OMA. When doping levels are relatively high, the increased

insertion loss starts to play the dominating role and leads to higher laser power consumption. **Another key observation is that the MS-MZM transmitter with 1 V driver are in fact more energy efficient than the transmitter with 2 V driver. Because the driver power dominates, the total power consumption for MS-MZM under the current technology and link constraints.** The optimized MS-MZM transmitter consumes 4.9 pJ/b at 50 Gb/s. More details about the optimization results can be found in Table IV.

### C. Traveling-Wave Mach Zehnder Transmitter

**The driver for traveling-wave MZM could potentially be more energy efficient at high data rates.** The output signal of the driver propagates along the on-chip electrode as shown in Fig. 19(b). In the optimized design, the RF and optical group velocities are matched. Any mismatch in them degrades the OMA and thus increases the total optimal transmitter energy. In our optimization engine, **such velocity matching condition is assumed to be satisfied for first-order system analysis.** The impact of mismatch can simulated in time domain through the proposed Simulink toolbox for specific designs [35].

The final stage of the driver can be a CML driver with load resistance  $R_L$ . The differential peak-to-peak output swing of the driver is denoted as  $V_{TW}$  and the attenuation coefficient of electrical signal on transmission is denoted as  $\alpha_t$ . In the optimization engine for TW-MZM,  **$\alpha_t$  is set based on the frequency-dependent measurement results in [24].** For 50 Gb/s modulation,  $\alpha_t$  corresponds to 2.5 dB/mm. Note that the effect of waveguide dopings on  $\alpha_t$  is neglected. As the voltage bias attenuates along the transmission lines, the effective modulation phase shift for TW-MZM can be derived as

$$\Delta\phi_{mod} = \frac{2\pi}{\lambda} \int_0^L [n_{\text{eff}}(-V(z)) - n_{\text{eff}}(V(z))] dz \quad (34)$$

$$V(z) = \frac{V_{TW}}{2} e^{-\alpha_t z} \quad (35)$$



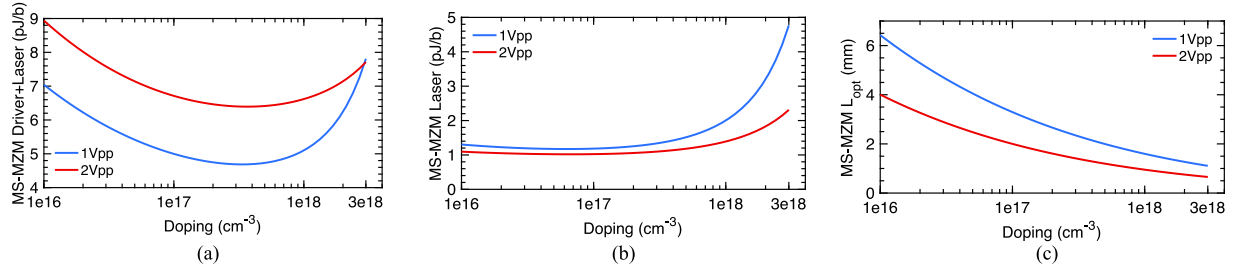


Fig. 20. Optimization results for multi-stage MZM transmitters at 50 Gb/s with two peak-to-peak voltage swings (1 V and 2 V). (a) the total transmitter E/b, (b) laser E/b, (c) the optimal arm length  $L_{opt}$ .

TABLE IV  
50 GB/S MZM OPTIMAL DESIGN PARAMETERS AND POWER (PJ/B)

	$V_{pp}$ (V)	Doping ( $\text{cm}^{-3}$ )	L (mm)	Laser	Driver	Total
MS	1.0	$3.3 \times 10^{17}$	2.3	1.4	3.3	<b>4.7</b>
MS	2.0	$3.7 \times 10^{17}$	1.3	1.1	5.3	6.4
TW	0.6	$6.1 \times 10^{17}$	2.8	4.5	1.2	5.7
TW	0.8	$3.0 \times 10^{17}$	1.4	3.5	1.6	<b>5.1</b>
TW	1.0	$2.0 \times 10^{17}$	2.0	3.2	2.0	5.2

where the effective index  $n_{\text{eff}}$  depends on the location  $z$  on the waveguide and the driver voltage  $V_{TW}$ . Based on the modified  $\Delta\phi_{mod}$ , the normalized OMA and ER for TW-MZM can thereby be calculated. Given the same link constraints as MS-MZM, the required laser energy-per-bit for TW-MZM  $E_{laser}$  can be calculated as well.

When a CML driver is used for the final stage with supply voltage  $V_{DD}$  and single-end swing  $V_{TW}/2$ , the driver energy-per-bit for TW-MZM can be calculated as

$$E_{dr,TW} = \frac{1}{\eta_d \cdot f_b} \cdot \frac{V_{TW}}{2(Z_0/2)} \cdot V_{DD} = \frac{V_{TW} V_{DD}}{\eta_d Z_0 \cdot f_b} \quad (36)$$

The effective load impedance of the parallel transmission lines is  $Z_0/2$ , and  $Z_0$  is assumed to be  $60 \Omega$  according to the typical transmission line design in [24]. The driver efficiency  $\eta_d$  is assumed to be 20% which accounts for power loss on load resistance  $R_L$  and any power consumed by the pre-drivers.

Under the same technology and link constraints, the optimization engine minimizes the total E/b for TW-MZM transmitter by finding the optimal arm length for different doping levels. For 50 Gb/s TW-MZM transmitter, co-optimizations are carried out for three different  $V_{TW}$  across the typical doping range as shown in Fig. 21. The optimization results show that laser power would dominate the total transmitter power and increase dramatically when doping levels are relatively low. From the optimization results, the optimal E/b for TW-MZM transmitter is achieved when the differential peak-to-peak voltage swing is around 0.8 V. Similar to MS-MZM, the optimal arm length of TW-MZM also decreases as the doping levels increase.

The optimal doping levels for MS-MZM and TW-MZM as well as their corresponding laser and driver power are listed in Table IV. At 50 Gb/s, the optimized TW-MZM tends to consume more laser power, whereas MS-MZM consumes more driver power. Overall, the optimized TW-MZM transmitter consumes around 5.1 pJ/b energy, slightly higher than the 4.7 pJ/b

consumed by the optimized MS-MZM transmitter. For both transmitter architectures, optimizing doping levels is crucial for achieving the best energy efficiency.

## VI. COMPARISONS

The optimization framework allows us to compare the energy efficiency of MRM and MZM optical transmitters including laser and driver power. PAM4 modulation is discussed as a potential way to mitigate the inherent optical bandwidth constraint for microrings. For Mach-Zehnder modulators, we have focused on NRZ modulation and analyzed both multi-stage and traveling-wave MZ-modulators. All the transmitters are optimized under the same technology and link constraints. The impact of doping levels for transmitter designs has been addressed in depth using the optimization framework.

For microring modulators, thermal tuning is essential for keeping the resonant frequency of microring locked to the laser frequency. Microring's thermal tuning can be done via an embedded microheater and a feedback mechanism. The heaters have been implemented in silicon or polysilicon to be more efficient and robust to electromigration. In a recent work [21], the thermal tuner for microrings achieves a 524 GHz ( $> 50^\circ\text{C}$  temperature) tuning range at  $3.8 \mu\text{W}/\text{GHz}$  consuming 2 mW in the heater driver and 0.74 mW in tuner logic. In order to estimate the thermal tuner power, ring's resonance has to be adjusted for the entire commercial temperature range (COM) in data-centers ( $0-70^\circ\text{C}$ ) leading to 3.5 mW. Therefore, the thermal tuning power for microrings are almost negligible compared to other link components at 50 Gb/s.

For the analysis above, we have set the link margin to 3 dB and assumed 3 dB coupler loss, 10% laser wall-plug efficiency and  $-10$  dBm receiver sensitivity for NRZ at 50 Gb/s. In practice, any deviation from these link constraints can be considered by adjusting the link margin. Now we consider three different link margins (0 dB, 3 dB and 6 dB) and show how the energy efficiency comparison would change between the different transmitter architectures at 50 Gb/s. The new energy breakdowns are shown in Fig. 22 with different link margins. For Mach-Zehnder modulators, the optimized multi-stage MZM transmitter can be more energy efficient than traveling-wave MZM transmitter when higher link margin is used. Because the MS-MZM uses significantly less laser power. If a smaller link margin or further relaxed link constraints are used, traveling-wave MZM may become more energy efficient. In this case, the

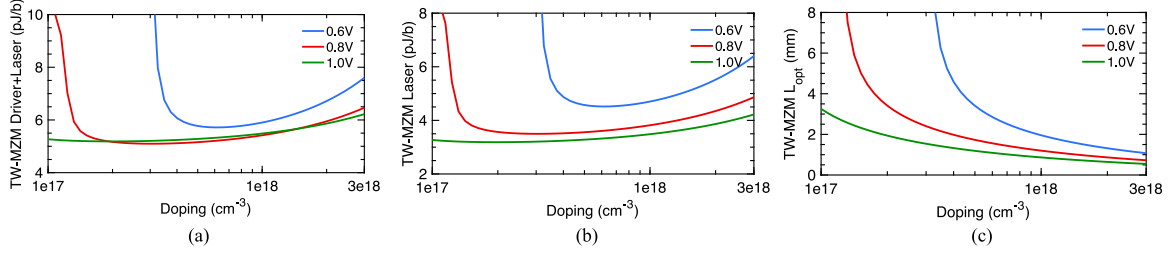


Fig. 21. Optimization results for traveling-wave MZM transmitters at 50 Gb/s with three differential peak-to-peak voltage swings  $V_{TW}$  (0.6, 0.8, 1.0 V). (a) the total transmitter E/b, (b) laser E/b, (c) optimal arm length  $L$ .

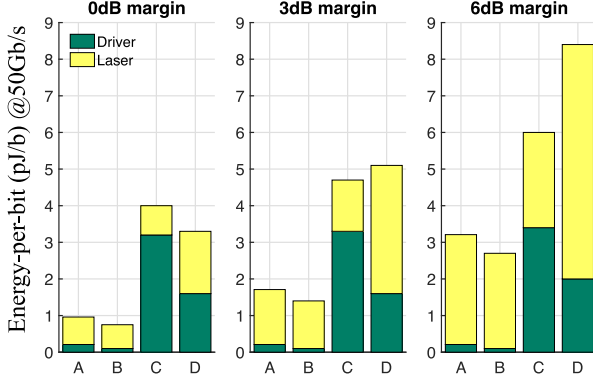


Fig. 22. Detailed energy breakdown and energy efficiency comparison between optimized (A) NRZ-MRM, (B) PAM4-MRM, (C) MS-MZM and (D) TW-MZM transmitters at 50 Gb/s. Three different link margins are considered: 0 dB, 3 dB and 6 dB.

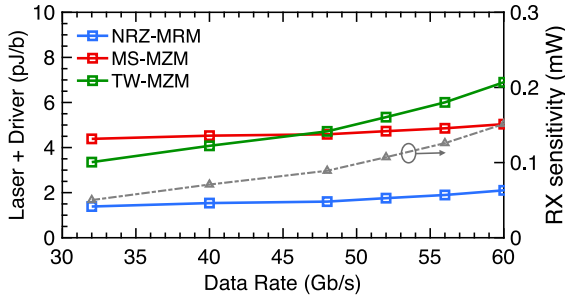


Fig. 23. Energy efficiency comparison between optimized NRZ-MRM, MS-MZM and TW-MZM transmitters at different data rates. The gray line shows the receiver sensitivity vs data rate according to measurement in [10].

driver energy takes up larger portion of total energy budget and the optimized traveling-wave MZM transmitter benefits from its relatively low driver E/b.

For 50 Gb/s NRZ optical links with a typical 3 dB link margin, MRM transmitters could save more than 60% of the total power compared to MZM transmitters when both are optimized through co-optimization framework. For microring modulators, switching to PAM4 modulation could further save around 20% total transmitter power from NRZ modulation. For all the cases here, we assumed a fixed receiver sensitivity, a fixed data rate and the same technology constraints from the same silicon photonic platform.

As the data rate increases, the sensitivity of the high-speed optical receivers would drop mainly due to the bandwidth limitations of the circuit blocks as shown in Fig. 23. In our

optimization framework, we set the receiver sensitivity based on the measurement results of the 65 Gb/s receiver design in 14 nm FinFet [10]. In addition to receiver sensitivity, the optical bandwidth of microrings and the transmission line loss also vary as the targeted data rate varies. The minimum E/b for transmitters using the optimized NRZ-MRM, MS-MZM and TW-MZM are obtained for 32–60 Gb/s, as shown in Fig. 23. Only NRZ links are considered limited to the available receiver sensitivity data. It is clear that the optimized microring modulator always consumes much less power than the optimized Mach-Zehnder modulator for the data rates of interest. This is generally due to the compact size of microrings. The optimizations at different data rate are also done under the same technology and link constraints.

## VII. CONCLUSION

This paper proposes a co-optimization framework for designing high-speed silicon photonic transmitters. The new framework integrates a simple but accurate compact model for optical phase shifters, analytical models for photonic modulators and a new Simulink simulation toolbox. It allows us to explore the design trade-offs in depth for microring and Mach-Zehnder optical transmitters and compare their performances given the same set of technology and link constraints. Our results show that silicon photonic links, especially microring-based links, have great potential to provide energy-efficient optical solutions for next-generation inter-rack and intra-rack links.

Although the paper does not go into circuit implementation details, it provides a useful co-optimization and verification framework for designing high-speed silicon photonic transmitters in the context of a practical optical link. This framework can be applicable to most of today's silicon photonic platforms that rely on PN junction based phase shifters. It can be extended to include receiver designs and thermal tuning designs, and assist the co-optimization of the next-generation silicon photonic interconnects.

## REFERENCES

- [1] H. Xu *et al.*, "High speed silicon Mach-Zehnder modulator based on interleaved PN junctions," *Opt. Express*, vol. 20, no. 14, pp. 15093–15099, 2012.
- [2] D. J. Thomson *et al.*, "50-Gb/s silicon optical modulator," *IEEE Photon. Technol. Lett.*, vol. 24, no. 4, pp. 234–236, Feb. 2012.
- [3] D. M. Gill *et al.*, "Demonstration of error free operation up to 32 Gb/s from a CMOS integrated monolithic nano-photon transmitter," *IEEE Photon. Technol. Lett.*, vol. 28, no. 13, pp. 1410–1413, Jul. 2016.

- [4] T. Baehr-Jones *et al.*, "Ultralow drive voltage silicon traveling-wave modulator," *Opt. Express*, vol. 20, no. 11, pp. 12014–12020, 2012.
- [5] Hui Yu, "Performance tradeoff between lateral and interdigitated doping patterns for high speed carrier-depletion based silicon modulators," *Opt. Express*, vol. 19, no. 12, pp. 11507–11516, 2011.
- [6] G. Li *et al.*, "Ring resonator modulators in silicon for interchip photonic links," *IEEE J. Sel. Topics Quantum Electron.*, vol. 19, no. 6, pp. 95–113, Nov. 2013.
- [7] N. Qi *et al.*, "A 25 Gb/s, 520 mW, 6.4 Vpp silicon-photonic Mach-Zehnder modulator with distributed driver in CMOS," in *Proc. Opt. Fiber Commun. Conf. Exhib.*, 2015, pp. 1–3.
- [8] C. Sun *et al.*, "Single-chip microprocessor that communicates directly using light," *Nature*, vol. 528, no. 7583, pp. 534–538, Dec. 2015.
- [9] K. T. Settaluri *et al.*, "Demonstration of an optical chip-to-chip link in a 3D integrated electronic-photonic platform," in *Proc. Eur. Solid-State Circuits Conf.*, 2015, pp. 156–159.
- [10] A. Cevero *et al.*, "A 65 Gb/s, 1.4 pJ/b NRZ optical receiver data-path in 14 nm CMOS FinFet," in *Proc. IEEE Int. Solid-State Circuits Conf.*, 2017, pp. 482–483.
- [11] G. Denoyer *et al.*, "Hybrid silicon photonic circuits and transceiver for 50 Gb/s NRZ transmission over single-mode fiber," *J. Lightw. Technol.*, vol. 33, no. 6, pp. 1247–1254, Mar. 2015.
- [12] M. Pantouvaki *et al.*, "50 Gb/s silicon photonics platform for short-reach optical interconnects," in *Proc. Opt. Fiber Commun. Conf.*, 2016, pp. 1–3.
- [13] M. Rakowski *et al.*, "A 50 Gb/s, 610 fJ/bit hybrid CMOS-Si photonics ring-based NRZ-OOK transmitter," in *Proc. Opt. Fiber Commun. Conf. Exhib.*, 2016, Paper Th1F4.
- [14] C. Xiong, D. Gill, J. Proesel, J. Orcutt, W. Haensch, and W. M. Green, "A monolithic 56 Gb/s CMOS integrated nanophotonic PAM-4 transmitter," in *Proc. Opt. Interconnects Conf.*, 2015, pp. 16–17.
- [15] X. Tu *et al.*, "50-Gb/s silicon optical modulator with traveling-wave electrodes," *Opt. Express*, vol. 21, no. 10, pp. 12776–12782, May 2013.
- [16] M. Streshinsky *et al.*, "Low power 50 Gb/s silicon traveling wave Mach-Zehnder modulator near 1300 nm," *Opt. Express*, vol. 21, no. 25, pp. 30350–30357, Dec. 2013.
- [17] X. Zheng *et al.*, "Efficient WDM laser sources towards terabyte/s silicon photonic interconnects," *J. Lightw. Technol.*, vol. 31, no. 24, pp. 4142–4154, Dec. 2013.
- [18] S. Moazeni *et al.*, "A 40 Gb/s PAM-4 transmitter based on a ring resonator optical DAC in 45 nm SOI CMOS," in *Proc. IEEE Int. Solid-State Circuits Conf.*, 2017, pp. 486–487.
- [19] I.-L. Gheorma and R. M. Osgood, "Fundamental limitations of optical resonator based high-speed EO modulators," *IEEE Photon. Technol. Lett.*, vol. 14, no. 6, pp. 795–797, Jun. 2002.
- [20] B. E. Little, S. T. Chu, H. A. Haus, J. Foresi, and J.-P. Laine, "Microring resonator channel dropping filters," *J. Lightw. Technol.*, vol. 15, no. 6, pp. 998–1005, Jun. 1997.
- [21] C. Sun *et al.*, "A 45 nm CMOS-SOI monolithic photonics platform with bit-statistics-based resonant microring thermal tuning," *IEEE J. Solid-State Circuits*, vol. 51, no. 4, pp. 893–907, Apr. 2016.
- [22] M. Georgas, J. Leu, B. Moss, C. Sun, and V. Stojanovic, "Addressing link-level design tradeoffs for integrated photonic interconnects," in *Proc. IEEE Custom Integr. Circuits Conf.*, 2011, pp. 1–8.
- [23] C. Sun *et al.*, "DSENT a tool connecting emerging photonics with electronics for opto-electronic networks-on-chip modeling," in *Proc. IEEE/ACM Int. Symp. New. Chip*, 2012, pp. 201–210.
- [24] E. Temporiti *et al.*, "Insights into silicon photonics Mach-Zehnder-based optical transmitter architectures," *IEEE J. Solid-State Circuits*, vol. 51, no. 12, pp. 3178–3191, Dec. 2016.
- [25] H. Bahrami *et al.*, "Time-domain large-signal modeling of traveling-wave modulators on SOI," *J. Lightw. Technol.*, vol. 34, no. 11, pp. 2812–2823, Jun. 2016.
- [26] G. Rasigade, D. Marris-Morini, M. Ziebell, E. Cassan, and L. Vivien, "Analytical model for depletion-based silicon modulator simulation," *Opt. Express*, vol. 19, no. 5, pp. 3919–3924, 2011.
- [27] Y. Ban, J.-M. Lee, B.-M. Yu, S.-H. Cho, and W.-Y. Choi, "Small-signal frequency responses for Si micro-ring modulators," in *Proc. Opt. Interconnects Conf.*, 2014, pp. 47–48.
- [28] L. Chrostowski and M. Hochberg, "Modulators" in *Silicon Photonics Design: From Devices to Systems*, 1st ed. Cambridge, U.K.: Cambridge Univ. Press, 2015.
- [29] C. Sorace-Agaskar, J. Leu, M. R. Watts, and V. Stojanovic, "Electro-optical co-simulation for integrated CMOS photonic circuits with VerilogA," *Opt. Express*, vol. 23, no. 21, pp. 27180–27203, Oct. 2015.
- [30] R. Soref and B. Bennett, "Electrooptical effects in silicon," *IEEE J. Quantum Electron.*, vol. 23, no. 1, pp. 123–129, Jan. 1987.
- [31] D. G. Rabus, *Integrated Ring Resonators*. New York, NY, USA: Springer-Verlag, 2007, Ch. 2.
- [32] B. Wang, K. Yu, H. Li, P. Y. Chiang, and S. Palermo, "Energy efficiency comparisons of NRZ and PAM4 modulation for ring-resonator-based silicon photonic links," in *Proc. IEEE 58th Int. Midwest Symp. Circuits Syst.*, 2015, pp. 1–4.
- [33] S. Palermo *et al.*, "PAM4 silicon photonic microring resonator-based transceiver circuits," *IEEE Int. Conf. Group IV Photon.*, Oct. 2015, pp. 153–154.
- [34] R. Dub-Demers, C. S. Park, S. LaRochelle, and W. Shi, "60 Gb/s PAM-4 operation with a silicon microring modulator," in *Proc. IEEE Int. Conf. Group IV Photon.*, Oct. 2015, pp. 153–154.
- [35] Developed Simulink toolbox. [Online]. Available: [https://github.com/igscal/SiPh\\_Simulink](https://github.com/igscal/SiPh_Simulink)
- [36] 100G PSM4 Specifications, PSM4-MSA. [Online]. Available: <http://www.psm4.org>
- [37] 100G CWDM Spec, CWDM4-MSA. [Online]. Available: <http://www.cwmd4-msa.org>

**Sen Lin** received the B.S. degree in microelectronics from Tsinghua University, Beijing, China, in 2012. He is currently working toward the Ph.D. degree in electrical engineering and computer science at the University of California, Berkeley, CA, USA. He worked as an intern and consultant at Xilinx, San Jose, CA, USA, in 2015 and 2016, where his work focused on the design of high speed PAM4 receiver and optical interconnects. In summer 2016, he worked as an intern in Ayar Labs, San Francisco, CA, USA, where he designed clocking circuits for high-speed optical transceivers. His research interests include modeling and design of integrated silicon photonic systems, high-speed optical transceivers, coherent communication systems, and mixed-signal integrated circuits.

**Sajjad Moazeni** received the B.S. degree from Sharif University of Technology, Tehran, Iran, in 2013, and the M.S. degree from the University of California, Berkeley, CA, USA, in 2016, both in electrical engineering. He is currently working toward the Ph.D. degree in electrical engineering and computer science at the University of California, Berkeley, CA, USA. He spent summer 2015 at Oracle America, Inc., in the mixed-signal design group. His research interests include integrated optics, silicon photonics, and analog/mixed-signal integrated circuits.

**Krishna T. Settaluri** received the B.Sc. and M.Eng. degrees from the Massachusetts Institute of Technology, Cambridge, MA, USA, in 2011 and 2012, respectively. He was a visiting researcher at the California Institute of Technology, Pasadena, CA, USA, until 2013, before joining the Ph.D. program at the University of California, Berkeley, CA, USA. Between 2012 and present, he served as a consultant for companies including Infinite Corridor Technology, Cambridge, MA, USA, and Chirp Microsystems, Berkeley, CA, USA. In summer 2016, he worked as an intern at Apple, Cupertino, CA, USA. Since fall 2016, he is employed in part-time with Ayar Labs, San Francisco, CA, USA. His current research interests include high-speed silicon photonic transceivers, high-bandwidth management techniques for WDM links, modeling and design of optical components and systems, and high-speed mixed-signal IC design.

**Vladimir Stojanović** received the Dipl.Ing. degree from the University of Belgrade, Belgrade, Serbia, in 1998, and the Ph.D. degree in electrical engineering from Stanford University, Stanford, CA, USA, in 2005.

He is an Associate Professor of electrical engineering and computer science with the University of California, Berkeley, CA, USA. He was also with Rambus, Inc., Los Altos, CA, USA, as a Principal Engineer from 2001 through 2004 and with the Massachusetts Institute of Technology, Cambridge, MA, USA, as an Associate Professor from 2005 to 2013. His research interests include design, modeling, and optimization of integrated systems, from CMOS-based VLSI blocks and interfaces to system design with emerging devices like NEM relays and silicon photonics. He is also interested in design and implementation of energy-efficient electrical and optical networks, and digital communication techniques in high-speed interfaces and high-speed mixed-signal IC design. He was an IEEE Solid-State Circuits Society Distinguished Lecturer for the 2012–2013 term. He received the 2006 IBM Faculty Partnership Award, and the 2009 NSF CAREER Award as well as the 2008 ICCAD William J. McCalla, 2008 IEEE Transactions on Advanced Packaging, and 2010 ISSCC Jack Raper Best Paper Awards.